Sediment transport and deposition on a river-dominated tidal flat: An idealized model study

Shih-Nan Chen,[1] W. Rockwell Geyer,[1] Christopher R. Sherwood,[2] and David K. Ralston[1]

[1]   A 3-D hydrodynamic model is used to investigate how different size classes of river-derived sediment are transported, exported and trapped on an idealized, river-dominated tidal flat. The model is composed of a river channel flanked by sloping tidal flats, a configuration motivated by the intertidal region of the Skagit River mouth in Washington State, United States. It is forced by mixed tides and a pulse of freshwater and sediment with various settling velocities. In this system, the river not only influences stratification but also contributes a significant cross-shore transport. As a result, the bottom stress is strongly ebb-dominated in the channel because of the seaward advance of strong river flow as the tidal flats drain during ebbs. Sediment deposition patterns and mass budgets are sensitive to settling velocity. The lateral sediment spreading scales with an advective distance (settling time multiplied by lateral flow speed), thereby confining the fast settling sediment classes in the channel. Residual sediment transport is landward on the flats, because of settling lag, but is strongly seaward in the channel. The seaward transport mainly occurs during big ebbs and is controlled by a length scale ratio L_d/X_{WL}, where L_d is a cross-shore advective distance (settling time multiplied by river outlet velocity), and X_{WL} is the immersed cross-shore length of the intertidal zone. Sediment trapping requires $L_d/X_{WL} < 1$, leading to more trapping for the faster settling classes. Sensitivity studies show that including stratification and reducing tidal range both favor sediment trapping, whereas varying channel geometries and asymmetry of tides has relatively small impacts. Implications of the modeling results on the south Skagit intertidal region are discussed.

1. Introduction

[2] Tidal flats are very low slope, largely unvegetated environments that are commonly found along mesotidal and macrotidal coasts. They are intertidal regions with a majority of their surface area exposed to air during low tides. They usually border landward with salt marshes and seaward with an embayment or an estuarine channel. External forces exerting on tidal flats include tides, river discharge, wind/waves, and baroclinicity generated by density contrasts [*Le Hir et al.*, 2000]. Governed by these temporarily varying forces, sediment transport processes on tidal flat therefore occur at multiple time scales, ranging from seconds to seasons [*Christie et al.*, 1999].

[3] Sediment transport processes on tidal flats are less well understood in comparison with those on either shallower salt marshes or deeper estuaries, partly because of logistic difficulties in field observations. However, there have been recent advances in this area. Sediment transport on tidal flats depends largely on the settling lag effect [*van Straaten and Keunen*, 1958; *Postma*, 1961]. Sediment particles that move during flood to an area of smaller tidal current velocity settle during slack tide. The settling needs time. During the ebbing tide, the particles experience a smaller velocity and do not return to their original location. The net effect of settling lag is a residual transport toward an area of lower energy. On the basis of this mechanism, many investigators have reported that during calm, tide-dominated periods, sediment flux on tidal flats is onshore [e.g., *Christie et al.*, 1999], even when the tidal current is known to be ebb-dominated (compare the Dollard estuary, *Dyer et al.* [2000]). This is because tidal current magnitude decreases landward, as the upper portion of the tidal flats is submerged for a progressively short period of flood tide [*Friedrichs and Aubrey*, 1996]. Integrating the onshore sediment flux over time, one would expect accretion on the upper flat, favoring a convex upward bottom slope. Such convex upward profile is commonly observed in tide-dominated environments [e.g., *Kirby*, 2000] and is morphologically stable (i.e., no divergence of bottom stress) so that the peak tidal current amplitude is largely uniform across the entire flat [*Friedrichs and Aubrey*, 1996; *Pritchard and Hogg*, 2003].

[1]Woods Hole Oceanographic Institution, Woods Hole, Massachusetts, USA.
[2]U.S. Geological Survey, Woods Hole, Massachusetts, USA.

[4] During windy, wave-dominated periods, in contrast, sediment fluxes are generally directed offshore. As surface waves propagate onshore, wave shoaling leads to a landward increase in wave height. This means that the maximum wave-induced bottom stress may locate at the upper or middle flat. Again through the settling lag effect, the seaward reduction in bottom stress then drives a net seaward sediment transport. A shifting transport pattern from onshore during calm periods to strongly offshore during storms has been observed from many intertidal regions, including by *Le Hir et al.* [2000] of the Seine estuary, by *Ralston and Stacey* [2007] and *Talke and Stacey* [2008] of San Francisco Bay, and by *Yang et al.* [2003] of the Yangtze River. For morphological responses, a bottom stress maximum at the upper or middle flat would cause local erosion, thereby favoring a concave upward bottom slope [*Friedrichs and Aubrey*, 1996; *Roberts et al.*, 2000].

[5] While the work above has provided insight into sediment transport processes on tidal flats, the forcing conditions and sediment sources are actually quite similar among the investigated systems. In those systems (mostly in Europe), sediment sources are either from offshore, supplied by a shore-parallel estuarine channel, or largely absent, and the external forces of interest are tide and wind/waves. Tidal flat systems in which the river provides significant sediment and flow energy inputs have not received much attention yet [*Le Hir et al.*, 2000]. Studies by *Ralston and Stacey* [2005] and *Ralston and Stacey* [2007] which focused on flow and sediment dynamics in a shallow mudflat channel are among the few exceptions. They demonstrated that such a shallow system can be highly stratified, with a small freshwater input from the channel upstream. The stratification modulated by tidal straining impacts sediment transport by suppressing turbulence and thus enhancing deposition during neap tides.

[6] Building upon the work by Ralston and Stacey, here we use a numerical model to study sediment transport across a similar type of tidal flat system in which river forcing is important. We use the intertidal region of the Skagit River mouth (Washington, United States) to define the parameters of the idealized model domain. Our system differs from Ralston and Stacey's in that the upstream river velocity is large compared to the tidal velocity. This means that the river not only affects water column stability through buoyancy input but also provides significant flow energy to the system. Our focus is on transport patterns associated with a freshwater discharge event (time scale of 5–10 days). The modeled tidal flat bathymetry is highly idealized, and only tidal forcing and a pulse of river and sediment discharge are considered. Specifically, we aim to explore and quantify (1) how different size classes of river-derived sediment (as represented by different settling velocities) are transported, exported and trapped and (2) how the interplay between river and tides controls the sediment trapping/export.

2. Methods

[7] We use the Regional Ocean Model System (ROMS) [*Haidvogel et al.*, 2000] to explore sediment transport on an idealized intertidal zone. The model geometry is scaled on the south Skagit intertidal region (see Figure 1 and *Yang and Khangaonkar* [2009]) but vastly simplified. The size of the intertidal zone is 6 km (cross-shore, x direction) by 5.4 km (along-shore, y direction) (Figure 1). It consists of a uniformly sloping tidal flat bisected by a single channel and connected to a deeper offshore basin. The slope of the tidal flat is 4 m over 6 km. The channel has a Gaussian cross-sectional shape with averaged width 210 m. The channel depth is 1 m, upstream of the intertidal zone (x > 6 km). When entering the intertidal zone, it decreases smoothly to become 0.5 m deeper than the flats over a cross-shore distance of 500 m. The grid configuration is $130 \times 73 \times 10$ (x-y-z). The intertidal zone is highly resolved, with a uniform Δx of 100 m and a stretched Δy that increases from 10 m in the channel to 420 m at the lateral boundaries. Outside of this area, the grid is telescoped in both the along- and cross-shore directions to provide a large receiving basin offshore and a long river channel. The vertical levels are also stretched to gain higher resolution near bottom and surface.

[8] The western boundary is closed, and 4 m mixed tides representative of the spring tide condition at the Skagit intertidal region is forced along the northern and southern boundaries of the offshore basin. We choose the case forced by symmetric mixed tides as the baseline condition and then modify the asymmetry and amplitude of the tides for sensitivity tests (see discussion). The symmetric, flood-dominated, and ebb-dominated tidal forcing are shown in Figure 1. Because the 4 m tidal range is equivalent to the elevation change of the flat slope (z = −2 and +2 at the seaward and landward edges, respectively), the entire flat region is exposed during the lower low tide. To simulate this wetting-drying process, a minimum water depth of 0.1 m is used as a "dry cell" criterion [e.g., *Warner et al.*, 2008]. The k-ε turbulence closure [*Jones and Launder*, 1972] with a stability function by *Kantha and Clayson* [1994] is used. The model results are however insensitive to the choices of turbulence closure. The seaward salinity open boundary conditions are implemented as by *Chen and Sanford* [2008] such that the offshore basin far from the buoyant plume maintains a constant salinity of 30 psu. A constant freshwater input representing a background discharge of 32 m^3 s^{-1} is initially imposed at the landward boundary. After the model flow field reaches a steady state, a 5 day pulse of freshwater is forced to simulate an annual flood event (2 day ramp-up/ramp-down with a peak of 138 m^3 s^{-1}). This forcing is consistent with the discharge to one of the south Skagit distributary channels during high-flow conditions.

[9] We vary the settling velocities to explore the sediment transport patterns for different size classes. Table 1 summarizes the numerical experiments. For each experiment, only one size class is used. The settling velocities range from 0.1 to 5 mm s^{-1}, bracketing sediment classes from fine silt (10 μm) to very fine sand (75 μm), according to Stokes' law. This range of settling velocities also encompasses typical clay-rich flocs and muddy aggregates. This size range covers over 60% of the suspended sediment load entering the south Skagit intertidal region (E. Grossman, personal communication, 2009). Medium and coarse sand that contribute to the rest of the load are not considered here. Since our focus is on the patterns and fate of sediment deposits derived from a flood event, for each size class there is initially no sediment on the bed, and the sediment enters the system with

Table 1. Sediment Parameters

	Fine Silt	Medium Silt	Medium Silt	Coarse Silt	Very Fine Sand	Very Fine Sand
w_s (mm s^{-1})	0.1	0.3	0.5	1	3	5
Critical shear stress (Pa)	0.05	0.05	0.05	0.06	0.085	0.1
Rouse number $(w_s/\kappa u_*)$[a]	0.01	0.03	0.05	0.1	0.3	0.5
T_{settle}/T_{tide}[b]	1.5	0.5	0.3	0.15	0.05	0.03

[a]u_* is calculated from the RMS bottom stress and averaged over the entire channel region ($u_* = 0.026$ and 0.008 m s^{-1} for channel and flats, respectively).

[b]$T_{settle} = H/w_s$ where $H = 1$ m; $T_{tide} = \omega^{-1}$ where ω is the tidal frequency.
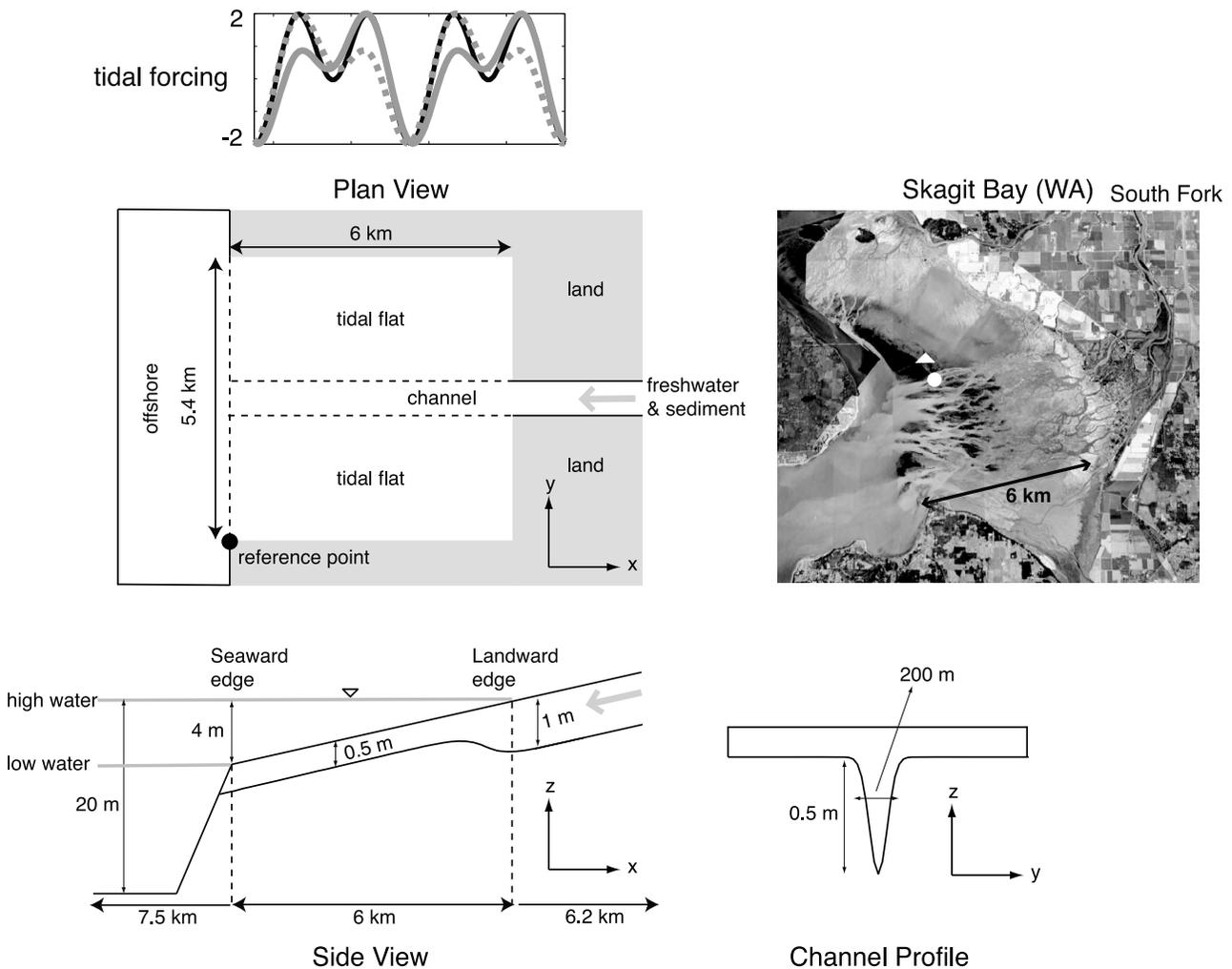
Figure 1. Idealized model domain. The intertidal zone consists of a river channel and broad tidal flats. The intertidal zone is 6 km and 5.4 km in cross-shore (x) and along-shore (y) direction, respectively. It connects to a 20 m deep offshore basin, and river and sediment discharges are specified upstream of the river channel. The origin of the coordinate system is chosen at the lower-left corner. The bottom slope is constant (4 m elevation over 6 km). Zero elevation (z = 0) is taken at the mean sea level that is at the midflat (x = 3 km). The channel depth shoals from 1 m to 0.5 m deeper than the flats over a cross-shore distance of 0.5 km. The channel shape is Gaussian, with an averaged width of 210 m. The spring tide forcing (4 m range) is shown on the top. The symmetric (baseline), flood-dominated, and ebb-dominated forcings are denoted by black, gray-dashed, and gray lines, respectively. Note that the domain geometry and channel profile are scaled disproportionately for better visualization. An aerial photo of the intertidal region of the Skagit River mouth in Washington (United States) is shown for reference.

the 5 day discharge pulse. We use the following sediment rating curve

$$C = C_{max}(Q_r/Q_{max})^b. \qquad (1)$$

where C is the suspended sediment concentration (kg m^{-3}) specified at the landward boundary, Q_r is the total discharge (m^3 s^{-1}), $C_{max} = 1$ kg m^{-3}, $Q_{max} = 138$ m^3 s^{-1}, and $b = 1.3$ (consistent with sediment yield estimates from the Skagit River, based on unpublished data from E. Grossman, personal communication, 2009). There is only one sediment bed layer. The erosion/deposition formulations and a constant erosion rate of 5×10^{-5} kg m^{-2} s^{-1} follow *Warner et al.* [2008]. With a depth-averaged velocity of 0.4 m s^{-1}, this erosion rate constant yields a suspended sediment concentration of 0.15 kg m^{-3} for w_s of 1 mm s^{-1}, which is consistent with field observations. We assume bed consolidation is negligible at the event time scale (5~10 days). The critical shear stress for each size class is determined based on Shields' diagram. For fine sediment classes ($w_s < 1$ mm s^{-1}), the Shields' diagram is less reliable, because of the cohesiveness of sediment particles. However, within this range, the model results are not sensitive to the changes in critical shear stress because sediment transport in the channel is limited by bed supply (see below).

3. Flow Characteristics

[10] The 4 m, symmetric mixed tides propagate as standing waves in the cross-shore direction (Figure 2). A mixed tide cycle consists of big flood, small ebb, small flood, and big ebb in sequence, according to sea level variations. On the flats, the maximum depth-averaged cross-shore velocity is 0.4 m s^{-1}, consistent with the theory of [*Friedrichs and Aubrey*, 1996] based on the slope of the flats and the tidal range. The flow on the flats is slightly ebb-dominated because of the presence of river discharge. Tidal nonlinearity [e.g., *Friedrichs and Aubrey*, 1988] is negligible here because of the short cross-shore domain length compared with tidal wavelength. Tidal asymmetry of the cross-shore flow is however sensitive to the external tidal forcing, switching to flood dominance when flood-dominated mixed tides are applied [e.g., *Hoitink et al.*, 2003]. In the channel, the cross-shore current is strongly ebb-dominated. The ebb dominance occurs as a result of conditions during the big ebbs (e.g., day 15.7–15.9) when the waterline retreats to the seaward edge of the intertidal zone and the flats are drained. Therefore, the strong ebb velocity is mainly contributed from the strong river flow (see below).

[11] The moving waterline with tides separates the flow in this system into two regimes. Landward of the waterline, the flow exhibits a fluvial regime. The flow is a seaward extension of the river. The momentum follows the classic Chezy balance ($(C_D U_r^2)/H = gS$ where C_D is the drag coefficient, H is the channel depth, S is bottom slope, and U_r is the river velocity). This means that the bottom stress scales with depth, and U_r varies with river discharge (i.e., changing depth), increasing from 0.7 to 1.2 m s^{-1} as the discharge ramps up. Note that the estimated river velocity of 1.2 m s^{-1} during peak discharge agrees with the strong ebb velocity in the channel in Figure 2b. Seaward of the waterline, the flow is within tidal regime, and the maximum cross-shore velocity is constrained by the theory of *Friedrichs and Aubrey* [1996]

(maximum tidal velocity U_t is 0.4 m s^{-1}). The alternation between tidal and fluvial regimes of the flow in the channel is consistent with the observation from the south Skagit intertidal region. From 19 to 25 June 2009, the tidal forcing on the Skagit progressed toward spring tide conditions (Figure 3a). As Figure 3b shows, the near-bed cross-shore velocities on the flats and in the channel were mostly constrained by U_t of 0.4 ms^{-1}. However, during the spring tide big ebb conditions (around days 22.5, 23.5, and 24.5), there were abrupt increases in ebb velocity. This happened when the instrument on the flats was out of water (i.e., missing data points). These features indicate the influence of the seaward extending fluvial regime. The consistency with observations lends confidence that the idealized model is able to represent the leading-order flow characteristics on the Skagit intertidal region.

[12] There are two main consequences of the velocity reduction from fluvial to tidal regime: first, the convergence of momentum drives along-shore flow (see below); and second, sediment being carried seaward would experience a large reduction in background flow energy, which then leads to sediment trapping (see section 5.3).

[13] A 2-D map of maximum bottom stress taken during the peak discharge clearly shows the ebb dominance (negative) for the entire domain, and the stress is much larger in the channel than on the flats (Figure 4, top). On the flats, the maximum bottom stress is quite uniform in the lower part of the flats (0~3 km) but decreases landward, consistent with *Friedrichs and Aubrey* [1996]. In the channel, the maximum bottom stress is uniform in the cross-shore direction. Again, this is not due to tidal processes but rather to the river outflow when the entire flats are drained. The maximum stress magnitude increases from 1.5 Pa during background conditions to 4 Pa during peak discharge.

[14] Lateral (along-shore) flow magnitude also shows marked tidal asymmetry. The depth-averaged lateral flow peaks during big floods, right after the sampling location is wetted (first gray shading in Figure 2c). Its magnitude can exceed 0.1 m s^{-1} during big floods, whereas during the rest of the tides the magnitude is on the order of 0.04 m s^{-1}. A plan view of velocity vectors taken during a big flood (Figure 4, bottom) shows that the enhanced lateral flow results from the convergence between flooding current and the strong seaward river flow. The enhanced lateral flow driven by convergence has important implications on lateral spreading of sediment (see section 5.1). Note that the slight asymmetry with respect to the channel axis in Figure 4 is due to the Earth's rotation.

[15] The system goes through a large salinity variation over every mixed tide cycle (Figure 2d), in a manner similar to that described by *Ralston and Stacey* [2005]. During big floods, a strong salinity front with an axial salinity gradient ($\partial s/\partial x$) of 0.05 psu m^{-1} advects landward. This sharp front is indicated by a peak in maximum buoyancy frequency at around day 15 in Figure 2d. After the passage of the front, the stratification shows a repeated pattern of increases during ebbs and decreases during floods. This pattern is consistent with tidal straining [*Simpson et al.*, 1990]. During floods, straining of isohalines aids bottom boundary layer mixing, leading to nearly vertical isohalines and thus weak stratification. During ebbs, the opposite pattern happens. The front moves seaward, and tidal straining stabilizes the water
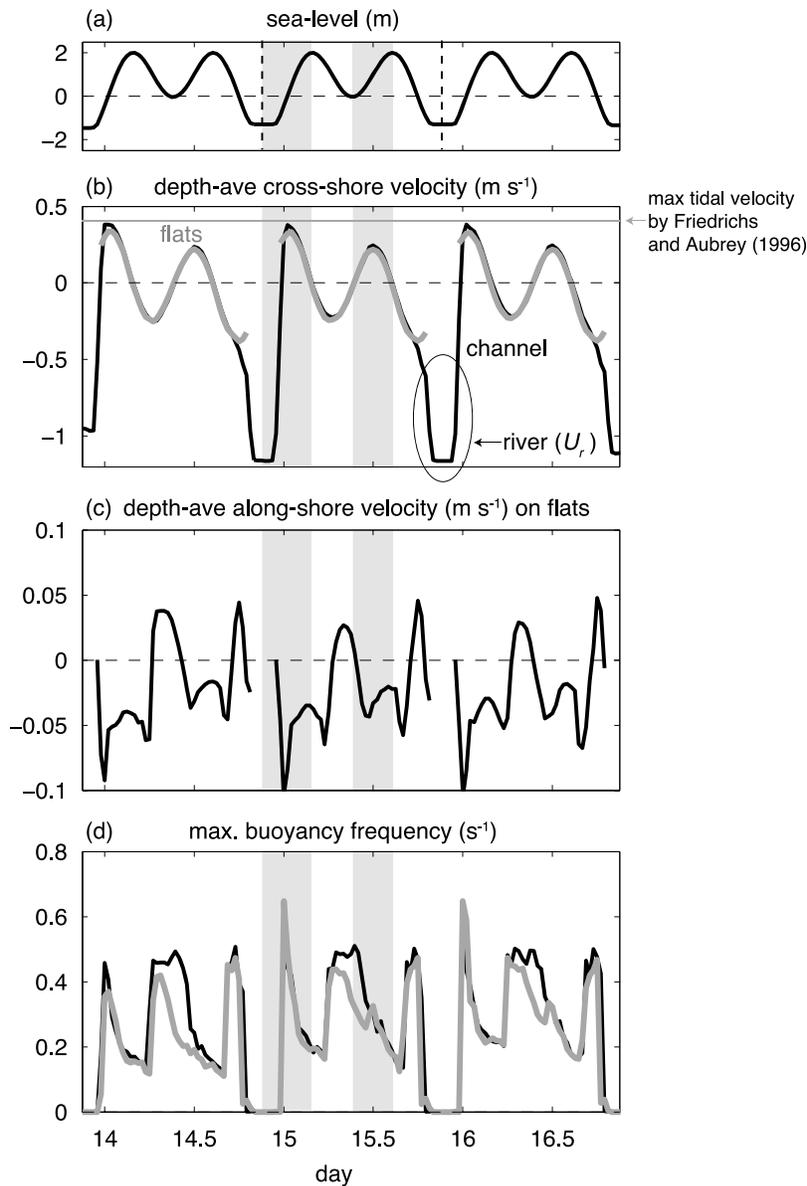
Figure 2. Three mixed tide cycles of (a) sea level, (b) depth-averaged cross-shore velocity, (c) depth-averaged along-shore velocity, and (d) maximum buoyancy frequency taken in a channel site (black line) and a location on the flats (gray line). These locations are marked by gray circle and triangle in Figure 4 (bottom). The 3 day period is during the peak discharge (whole 5 day event is from days 13–18). Two gray shadings indicate big and small flood.

column, promoting stratification. The strong stratification that is sustained over the early stage of the big ebbs has a significant impact on sediment trapping (see section 5.4). Around the middle of the big ebbs, mixing is strong enough to overcome straining, and the water column rapidly become well-mixed.

[16] Two dimensionless numbers relevant to the sediment dynamics on the intertidal zone are the Rouse number and a time scale ratio (Table 1). The Rouse number (R_o), a ratio of downward settling and upward turbulent diffusion, is the parameter determining the vertical sediment distribution. Within the range of settling velocities of interest, R_o is smaller than 0.3 for all but the two sand classes, indicating, in the absence of stratification, nearly uniform sediment concentration profiles for the finer sediment classes. The other rel-

evant parameter is the ratio of vertical settling time to the tidal time scale: $H\omega/w_s$, in which H is the characteristic depth (1 m here), w_s is settling velocity, and ω is tidal frequency (rad s^{-1}). The ratio is mostly smaller than 1, indicating that the sediment transport time scale is controlled by vertical settling except for finest particles, for which the settling time scale is comparable to the tidal time scale.

4. Results

[17] We first describe the patterns of sediment deposition at the end of the discharge event (day 18). The spatial distribution of deposition is strongly dependent on the sediment settling velocity, both with respect to the cross-shore distri-
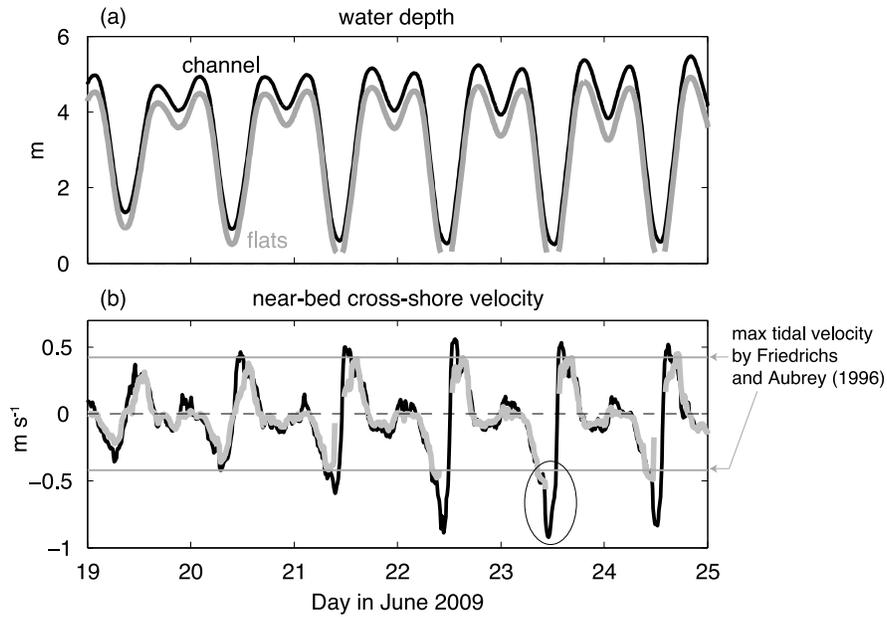
Figure 3. Time series of (a) water depth and (b) near-bed (0.25 m above bottom) cross-shore velocity taken in a channel site (black line) and a location on the flats (gray line) from 19 to 25 June 2009. These locations are marked by a white circle and triangle in the aerial photo of the Skagit Bay of Figure 1. During this period, the tidal forcing on the Skagit intertidal region progressed toward spring tide conditions. In Figure 3b, two gray horizontal lines indicate the maximum tidal velocity given by *Friedrichs and Aubrey*'s [1996] theory. The oval indicates the influences of the Skagit River.
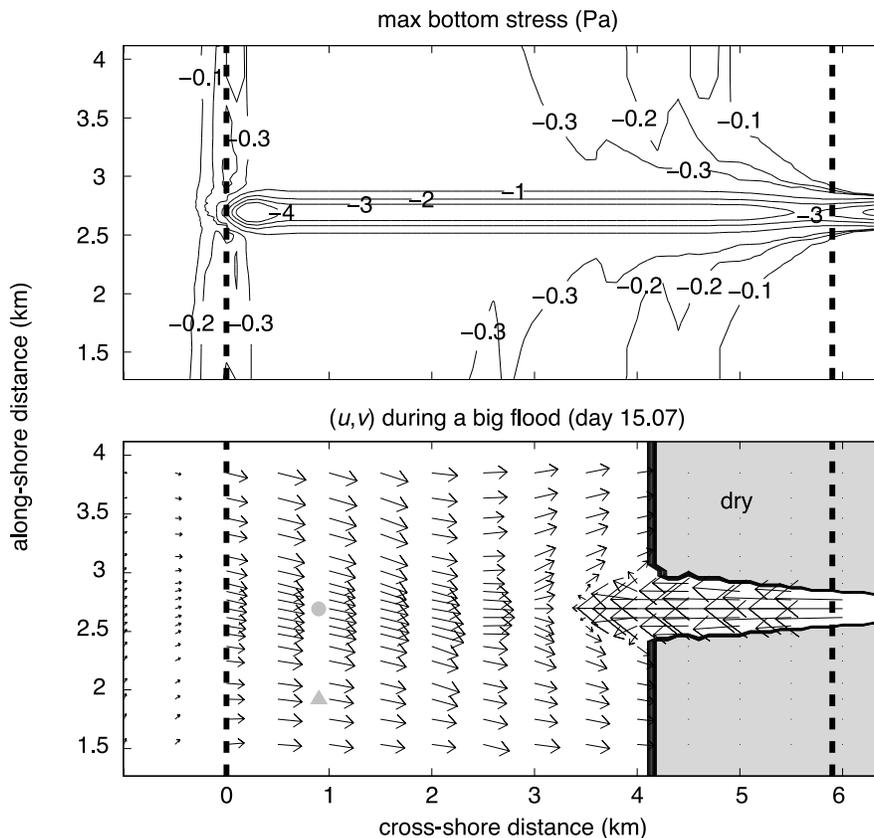
Figure 4. (top) Spatial distribution of maximum bottom stress. Negative values indicate ebb dominance of stress. (bottom) Snapshot of depth-averaged (u, v) during big flood. The gray circle and triangle indicate the channel and flat locations where the time series of Figure 2 is taken.

Figure 7. Time evolution of the integrated sediment mass for w_s of 0.1, 0.5, 1, and 5 mm s^{-1} (left to right). The total sediment input denoted by thin black lines is computed at the landward boundary of the intertidal zone (x = 6 km in Figure 1). The thick gray line is the total mass (including bed and water column) on the intertidal zone (channel + flats). The thick solid and dashed black lines denote the total mass in the channel and on the flats, respectively. The difference between input and mass on intertidal zone (gray) is the sediment export to the offshore basin. The vertical line in each panel denotes the end of the discharge event.

around x = 3 km. Landward of the waterline, channel is within the fluvial regime, and the channel sediment bed is completely scoured by strong river flow. Seaward of the waterline, the flats are submerged and the current is weak (e.g., day 15.2–15.7 in Figure 2b). Thus, the sediment-laden river discharges into quiescent water, leading to rapid sediment accumulation seaward of the waterline. During big ebbs, the waterline and river outlet move seaward, eroding and exporting the sediment that had previously deposited in the channel. The erosion only happens in the central part of the channel.
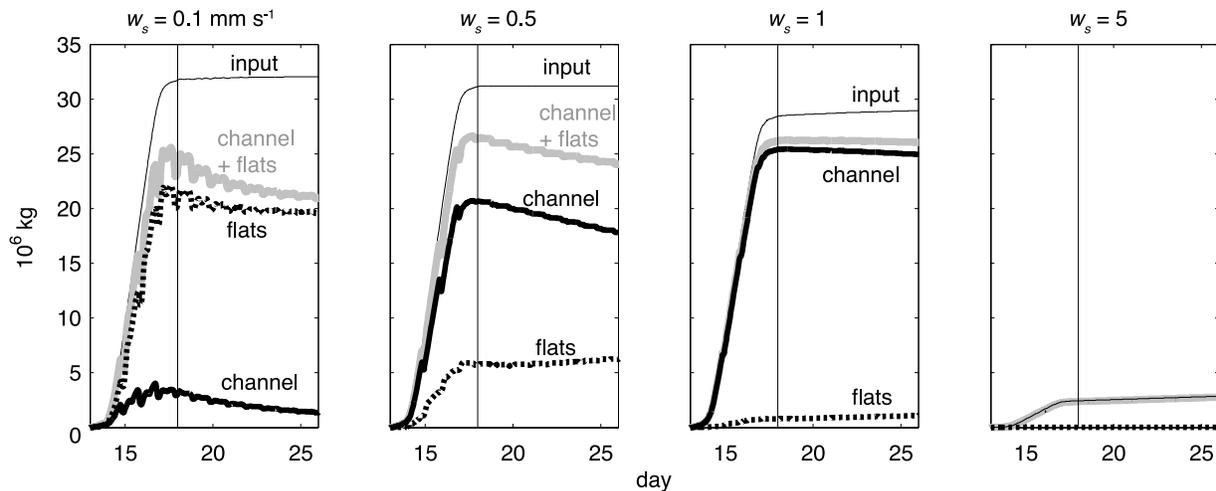
[19] For the higher-settling velocity case (w_s = 1 mm s^{-1}), in contrast, sediment accumulation happens mainly in the channel. During big floods, the waterline and river outlet move upstream, depositing sediment along its path in the channel. A small amount of sediment is dispersed onto the flats, as shown in Figure 5, but much smaller than can be resolved at the mm scale shown in Figure 6. During small ebbs and floods, the sediment-laden river again creates a thick deposit at x = 2–4 km. However, the footprint of this deposition zone is much smaller than that in the w_s of 0.1 mm s^{-1} case because of a shorter settling time. During big ebbs, the waterline and river outlet move seaward, carrying a small amount of bed mass eroded from the upper channel downstream. The integral effect is that the total sediment input largely stays in the channel, strongly contrasting the completely scoured channel in the w_s of 0.1 mm s^{-1} case.

[20] Time series of integrated sediment mass provide a more quantitative view on how the sediment distribution evolves with time (Figure 7). We divide the domain into three regions: channel, flats, and offshore basin. Input denotes the sediment supply entering the domain with river discharge (flux computed at x = 6 km). The stresses are high enough in the river upstream of the intertidal zone (i.e., x > 6 km) that there is essentially no deposition there for all but the sand size class. However, for those cases (e.g., w_s of

5 mm s^{-1}), significant deposition occurred within the upstream river channel during the event, reducing the input rate at the edge of the intertidal zone but providing a continued source after the event. Most of the sediment movement takes place during the event when the flow is most energetic. The rates at which sediment redistributes among different regions are relatively small afterward.

[21] Relative mass distribution among the flats and channel is sensitive to settling velocity, as noted above. Sediment mass is larger on the flats than in the channel for w_s of 0.1 mm s^{-1}, but this pattern reverses for greater settling velocities (Figure 7). As a result, the channel portion of the total mass on the intertidal zone increases monotonically with settling velocity. For $w_s \geq 1$ mm s^{-1}, essentially all of the sediment is confined in the channel. Overall, under tidal and river forcing, the intertidal zone behaves as an efficient sediment trap. Over 70% of the total input remains on the intertidal zone at the end of the event (see the baseline case in Table 2), and there is still over 60% of input remaining 10 days after the end of the event. The percentage of sediment trapping increases monotonically with settling velocity (Table 2).

5. Analysis and Discussion

5.1. Sediment Deposition on the Flats

[22] Sediment deposition on the upper flats (compare Figure 5) results from the reduced bottom stress there. *Postma* [1961] demonstrated that, with a settling lag effect, net sediment transport is toward the direction of decreasing bottom stress. *Schuttelaars and de Swart* [1996] and *de Swart and Zimmerman* [2009] obtained an analytical solution for the settling-lag mechanism. They show that the residual sediment flux due to settling lag can be expressed as

$$\langle uC \rangle = -\frac{3}{4}\left(\frac{\alpha u^3}{\gamma}\right)\frac{du}{dx}\frac{1}{\omega}F(T_{settle}/T_{tide}) \qquad (2)$$

Table 2. Sediment Mass Budget and Transport Rate for Various Numerical Experiments

	Percent of Sediment Trapping[a]				Event-Averaged Transport Rate (kg s^{-1})[b]			
	$w_s = 0.1$	0.5	1	5	$w_s = 0.1$	0.5	1	5
Baseline	72	85	92	97	17 (13)[c]	14 (13)	6 (6)	0.17 (0.17)
Homogeneous[d]	44	65	83	93	37 (23)[c]	24 (22)	10 (9)	0.37 (0.36)
Neap tide[e]	94	99	100	100	3.8	0.005	0	0
Flood-dominated[f]	79	85	91	97	14	12	6	0.19
Ebb-dominated[g]	74	79	91	97	17	16	7	0.19
Narrow, deep channel[h]	70	83	85	91	20	12	11	0.54
Shallow, wide channel[i]	67	87	96	98	22	10	3	0.06

[a](Intertidal zone mass)/input × 100; input equals intertidal zone mass plus offshore mass; intertidal zone mass equals channel mass plus tidal flat mass.
[b]Transport rate is computed at the seaward edge of the intertidal zone.
[c]Values within the parentheses indicate the channel portion of the transport rate.
[d]Differ from the baseline case by using constant salinity for the whole domain.
[e]Differ from the baseline case by using 2 m tide.
[f]Differ from the baseline case by using flood-dominated mixed tide (same tidal range; the gray dashed line in Figure 1).
[g]Differ from the baseline case by using ebb-dominated mixed tide (same tidal range; the gray solid line in Figure 1).
[h]Differ from the baseline case by using 1 m deep channel with an averaged width of 100 m.
[i]Differ from the baseline case by using 0.4 m deep channel with an averaged width of 400 m.

in which α is an erosion parameter, $1/\gamma$ is the settling time, $\alpha u^3/\gamma$ can be considered as the maximum tidal sediment flux, ω is the tidal frequency, and F (≥ 0) is a shape function depending on $T_{\text{settle}}/T_{\text{tide}}$. There are two important characteristics of the settling lag equation: first, the shape function F approaches zero at zero and infinite $T_{\text{settle}}/T_{\text{tide}}$. This means that there is no residual sediment transport when sediment particles sink instantaneously at slack tides or have a negligible settling velocity (i.e., behave like conservative water parcels); second, the residual transport is toward lower velocities (negative du/dx). In our system, the maximum bottom stress is largely uniform on the lower flats but decreases landward

of the midflats (Figure 4, top). We therefore anticipate a landward residual sediment transport on the flats.

[23] We compute the residual transport ($\langle q \rangle$: kg s^{-1}) during the event by

$$q = \iint u \cdot C \cdot dydz$$

$$\langle q \rangle = \frac{1}{T} \int q \cdot dt \tag{3}$$

where q is the tidal transport, u is cross-shore velocity, T covers 4 mixed tide cycles during the event, and $\int dydz$ is
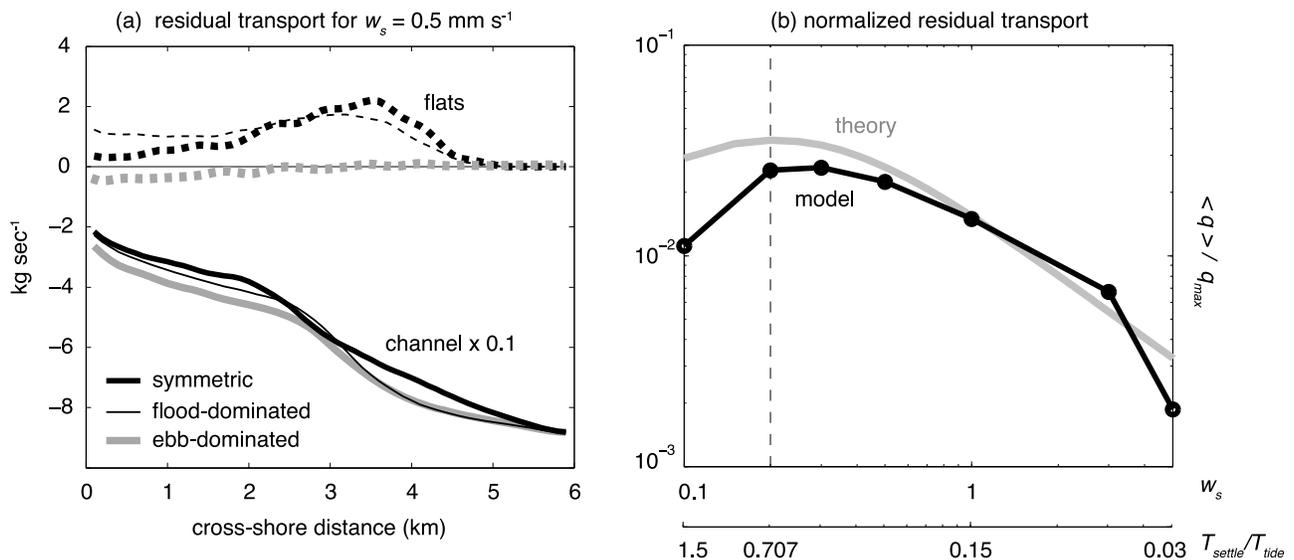
Figure 8. (a) Cross-shore profiles of residual sediment transport (kg s^{-1}) on the flats (dashed lines) and in the channel (solid lines) for ws of 0.5 mm s^{-1}. Symmetric, flood-dominated, and ebb-dominated tidal forcings (compare Figure 1) are denoted by thick, thin, and gray lines, respectively. The magnitude of the channel transport is scaled by a factor of 0.1 for better visualization. (b) Comparison of cross-flat transport to settling lag model of *Schuttelaars and de Swart* [1996] for different settling velocities. The black line is the model-derived cross-flat residual sediment flux, normalized by the maximum tidal sediment flux (equation (3)), and the gray line is the analytical solution. The vertical dashed line indicates the maximum residual sediment flux from the settling lag prediction. The second x axis shows $T_{\text{settle}}/T_{\text{tide}}$ for reference.

Figure 9. Lateral spreading (width) of the deposition plotted against settling velocity. The width of the deposit is calculated as square root of the lateral variance and is denoted by the black line. The gray dashed line is an advective dist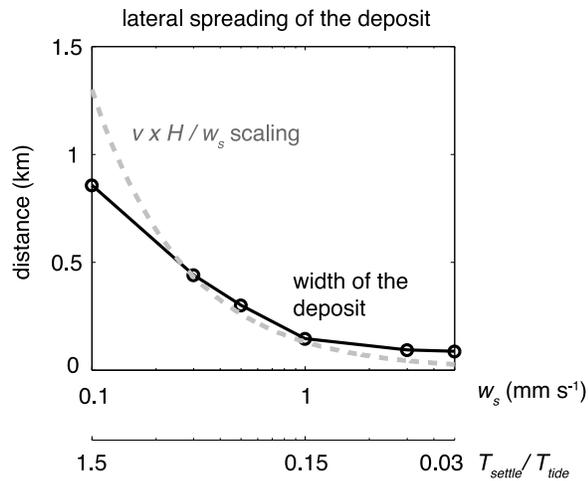ance scaling (vH/ws; v is 0.12 m s^{-1}, H is 1 m). The second x axis shows $T_{\text{settle}}/T_{\text{tide}}$ for reference.

the cross-sectional area of the flats or channel. As Figure 8a shows, the residual transport is seaward in the channel and landward on the flats (thick black lines). The transport in the channel is an order of magnitude larger than on the flats, consistent with the flat-channel bottom stress difference in Figure 4 (top). The transport on the flats peaks at the midflat and then decreases toward shore. The transition from divergence to convergence in $\langle q \rangle$ indicates sediment movement from middle to upper flats, creating the upper-flat deposition zone.

[24] The model-derived residual flux agrees reasonably well with the settling-lag equation of *Schuttelaars and de Swart* [1996] (Figure 8b). The residual flux is normalized by maximum tidal flux averaged over the upper flat. The normalized magnitude (i.e., the proportion of residual to tidal flux) is well predicted, and the model-derived and theoretical fluxes show a similar sensitivity to settling velocity. The consistency between model and theory supports the idea that the residual landward transport on the flats is driven by the settling lag effect under the symmetric tidal forcing. However, asymmetric tidal forcing also affects residual transport on the flats. In Figure 8a, the profiles of residual transport are similar between symmetric and flood-dominated cases, except the flood dominance induces additional landward transport at the lower flats (x = 0~2 km). Under ebb-dominated tides, in contrast, the magnitude of landward transport on the upper flats is greatly reduced, and the net transport switches to seaward at the lower flats. The reduced landward transport is likely due to a combination of limited sediment supply on the upper flats and the competing effects between settling lag and ebb-dominated tides. The limited upper-flat supply is intrinsic to ebb-dominated tides because the waterline during big floods only reaches the midflat (x = 4 km) and thus confines the lateral sediment spreading and deposition at the lower flats. Nevertheless, the asymmetry of tidal forcing only has minor impacts on the transport in channel and thereby has rather small effects on the overall

sediment budget (see section 5.5). It is also worth noting that the upper-flat deposition would cause the morphology to evolve toward a convex upward slope if there were no competing sediment transport processes.

[25] Next, we look at the patterns of the upper-flat deposition. It is clear in Figure 5 that the lateral spreading is larger for slower settling sediment. We characterize the lateral spreading by the width of the patch (as quantified by the square root of the lateral variance), and its sensitivity to settling velocity is shown in Figure 9. As can be seen, spreading increases monotonically as settling velocity decreases. An advective length scaling of vH/w_s (v of 0.12 m s^{-1} is the maximum lateral velocity averaged across the flat; H is 1 m) largely captures this relationship, suggesting that the lateral spreading is set by the distance a particle can travel before settling out. The simple scaling and the model-derived spreading begin to diverge when w_s approaches 0.1 mm s^{-1}. This is when the vertical settling and tidal time scales are comparable ($T_{\text{settle}}/T_{\text{tide}} \sim 1.5$; Table 1), meaning that lateral sediment transport could be limited by changes of tidal phase.

5.2. Sediment Accumulation in the Channel

[26] One of the distinct features of the deposition patterns shown in Figure 5 is the fine sediment is largely scoured while coarse sediment settles in the channel. The comparably more channel accumulation for the coarser sediment is due to a combination of a shorter lateral advective distance that confines the lateral sediment spreading and a larger depositional flux that scales with settling velocity. The sediment distribution in the channel is spatially variable. For example, in the cross-channel direction, the bottom stress peaks in the channel center. Thus, the channel center is largely scoured or has thinner deposits than on the sides (Figure 5). The integrated effect over time is to make the channel deeper and narrower in order to increase bottom stress and Q_s (see section 5.5). Additionally, in the along-channel direction, the averaged bottom stress decreases seaward because of the decreasing duration of river influence. The seaward stress reduction then leads to seaward decrease in the residual transport rate (compare Figure 8a). This means that sediment is moved from the upper to lower portion of the channel. The sediment export to the offshore basin is however determined by the conditions near the seaward edge of the domain, which we explore next.

5.3. Export Mechanisms

[27] The sediment budget indicates that a majority of the sediment input during a discharge event is trapped on the intertidal zone (channel + flats), and that trapping increases with settling velocity (Table 2, Figure 7). Here we explore in detail the trapping efficiency and mechanism for sediment export offshore.

[28] Sediment export occurs primarily in the channel. We compute the event-averaged transport (equation (3) but averaging over the event period) over the domain cross section at the seaward edge of the intertidal zone (Table 2). It can be seen that the averaged transport is seaward (positive) and decreases with increasing settling velocity. The channel contributes over 70% of the total seaward flux, because of its larger bottom stress compared to the flats.

[29] Instantaneous transport in the channel over a mixed tide cycle reveals that the export begins at big ebbs and
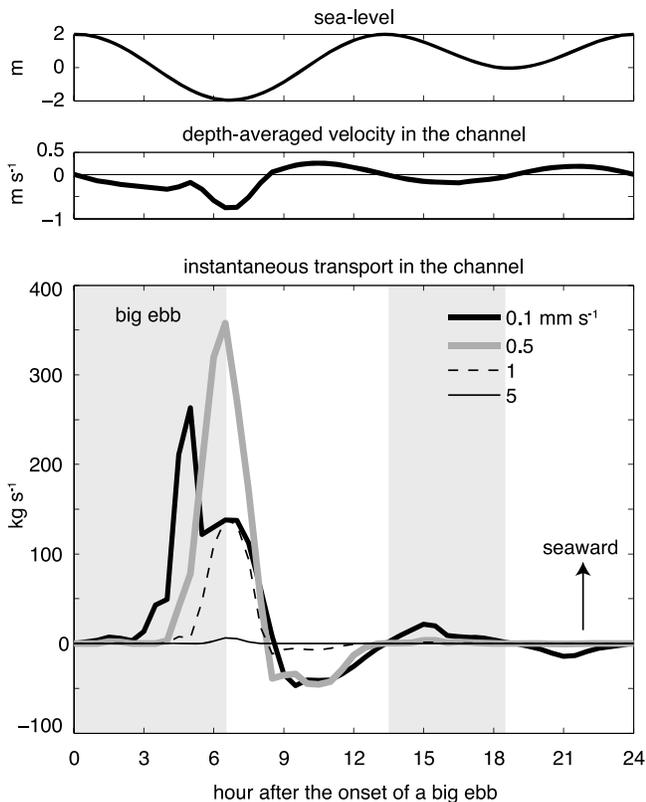
Figure 10. (bottom) Time series of transport in the channel for a typical mixed tide cycle during peak discharge, taken at the seaward edge of the intertidal zone. Different lines indicate different settling velocities. The instantaneous transport (q) is calculated by equation (3), and minus q is plotted here, so positive values indicate seaward transport. Two gray shadings indicate big and small ebb. (top and middle) Sea level and depth-averaged velocity (negative means seaward) in the channel for reference.

continues into early stage of big floods (Figure 10). This is when the flats are drained and the channel exhibits a fluvial regime (in effect, it becomes an extension of the river, with surface slope roughly matching bottom slope), with large bottom stress. There appears to be a time delay in the onset of export, which increases with faster settling velocity. To further investigate the timing of export with respect to settling velocity, we compare the cross-shore profiles depth-averaged U and sediment concentration in the channel during a big ebb for two settling velocities (Figure 11). The vertical line indicates the location of the waterline (X_{WL}) at 3.5 h after beginning of a big ebb. Seaward of X_{WL}, the depth-averaged U starts to decelerate when the sediment-carrying river flow meets the receiving tidal water. Note that the suspended sediment extends farther seaward than the elevated velocity, because of the finite settling time. The sediment concentration decreases seaward over a characteristic length scale L_d, with a shorter-length scale for w_s of 1 mm s^{-1} than for w_s of 0.1 mm s^{-1} because of faster settling. The difference in the settling distance (L_d) then leads to different time delays in the onset of export and more importantly sets the magnitude of export (see below).

[30] It can be inferred from Figure 11 that sediment export requires the settling distance larger than the cross-shore distance between the waterline and the edge of the intertidal zone, indicated as X_{WL} in Figure 11. The export criterion is then $L_d/X_{WL} > 1$. We can characterize the settling distance L_d of a given sediment class via the laterally averaged first moment

$$L_{d,y} = \frac{\int |x - X_{WL}| \cdot C(x,y,t)dx}{\int C(x,y,t)dx}$$
$$L_d = \frac{1}{B} \int_{channel} L_{d,y}dy \tag{4}$$

where x is the location downstream of X_{WL}, C is the depth-averaged concentration, and B is the channel width. Equation (4) accounts for both sediment input from upstream and from the bed. We then compare the time evolution of L_d/X_{WL} and sediment transport rate in the channel q (equation (3)) during a big ebb. w_s of 0.5 mm s^{-1} is taken as a representative example. As anticipated, sediment export does not occur for $L_d/X_{WL} < 1$ (4 h after the big ebb begins in Figure 12a) because sediment settles out before reaching the edge. As the ebb tide progresses, X_{WL} decreases with the waterline retreating seaward. When the export criterion of $L_d/X_{WL} > 1$ is met, export starts to increase and is correlated with L_d/X_{WL}.

[31] The percentage of total export is found to have the same dependence on settling velocity as the settling distance L_d (Figure 12b) because L_d describes how much sediment can be carried off the intertidal zone. Note that the time-averaged settling distance varies from 2.7 km for $w_s =$ 0.1 mm s^{-1} to just over 100 m for $w_s = 5$ mm s^{-1}. During neap tides (2 m tidal range), the minimum immersed cross-shore length of the intertidal zone, as indicated by the dashed horizontal line, always exceeds the settling distance for the faster settling sediment. This results in trapping of all of the coarse sediment (w_s over 0.5 mm s^{-1}; see section 5.5). The settling distance is found to be consistent with the simple advective scaling;

$$L_d \approx U_r H / w_s \tag{5}$$

where U_r is the river outlet velocity; H is the channel depth of 0.5 m. The smallest size class does not following this scaling, because of the influence of tidal time-dependence, as mentioned earlier in context with lateral spreading.

[32] Using equation (5) and the Chezy balance (section 3), we can rewrite L_d/X_{WL} for a system with linear slope as

$$\frac{L_d}{X_{WL}} = \left(\frac{4g}{C_D}\right)^{\frac{1}{2}} \frac{S^{\frac{3}{2}}S^{\frac{3}{2}}}{(A_0 - A)w_s} \tag{6}$$

where A_0 is the tidal flat elevation (4 m here), A is the tidal range and S is the bottom slope. This means that, for a fixed geometry, the export as controlled by L_d/X_{WL} decreases with increasing settling velocity and decreasing tidal range. This is because increasing settling velocity reduces the advective distance (L_d), whereas decreasing tidal range increases the distance between the waterline (X_{WL}) and the edge of the intertidal zone.
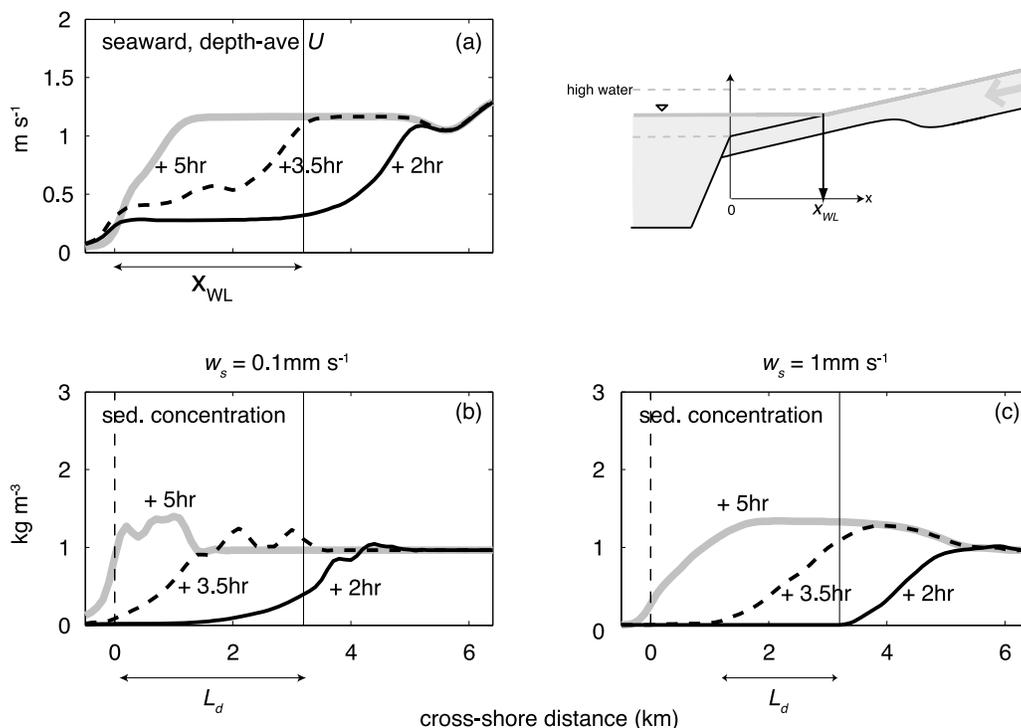
Figure 11. Cross-shore profiles of (a) depth-averaged cross-shore velocity and (b, c) suspended sediment concentration, taken along the channel center. Figures 11b and 11c are the scenarios with $w_s = 0.1$ and 1 mm s^{-1}, respectively. In each panel, there are three profiles, denoted by black, dashed, and gray lines. They are taken at 2, 3.5, and 5 h after the beginning of a big ebb during peak discharge. In Figure 11a, X_{WL} is the location of waterline for the 3.5 h profile. X_{WL} also represents the immersed, cross-shore length of the intertidal zone, which can be seen in the schematic on the upper right corner. In Figures 11b and 11c, L_d represents the settling distance, referenced to the instantaneous location of the waterline (equation (4)). The vertical dashed lines denote the seaward edge of the intertidal zone (x = 0).

5.4. Influence of Stratification

[33] We use cases with and without salinity contrast to evaluate the influences of stratification on sediment export and trapping. The homogeneous cases export more sediment than the stratified ones, and the magnitude of seaward transport in the channel increases 1.5 fold without stratification (Table 2). Comparing the instantaneous transport in the channel shows that the effects of stratification manifest before and after the major export pulse (Figure 13a). During the major export pulse (hours 4–8), the homogeneous and stratified cases are nearly identical, suggesting that the major pulse is barotropic. This is when the flats are drained and the river extends to the seaward edge (small X_{WL}) for efficient export. However, during the early ebb for the stratified case, the bottom stress is greatly reduced, and the seaward sediment transport is inhibited because of stratification. After the pulse (hours 8–12), the stratified cases have a larger import of sediment. The larger import is however not owing to the bottom stress differences. Instead, it is due to the availability of more bed sediment in the channel, which results from trapping during the early part of the previous ebb. Therefore, stratification contributes to sediment trapping in two related ways: first, it limits export during big ebbs by reducing bottom stress. Then, the sediment trapping during the ebb provides a larger supply to be carried landward by the subsequent flood.

[34] It is interesting to note the similarity of the sediment trapping criterion between estuaries and intertidal zones with tidal river channels. Sediment trapping can result from suspended sediment being advected over a turbulence-inhibited region, with the excess settling flux leading to trapping [*Geyer et al.*, 2004]. The horizontal gradient of turbulence could be due to a barotropic flow deceleration or an increase in stratification. For partially mixed estuaries, the stratification effect prevails [*Geyer*, 1993]. For intertidal zones, on the other hand, both barotropic and stratification effects occur, as shown in Figure 13. However, the stratification effect is comparably weaker because of the shallow depth of the intertidal zone (i.e., small baroclinic velocity compared with river and tidal velocities). The trapping criterion is therefore dependent on a mismatch between advective distance ($U_r H/w_s$) and the cross-shore distance between the barotropic convergence (X_{WL} here) and the edge of the intertidal zone.

[35] Note that barotropic trapping requires a large ratio of river to tidal velocity (U_r/U_t). In a system with relatively weak river outflow, *Ralston and Stacey* [2007] showed that stratification effects were more important than barotropic. They found that increased stratification during ebbs enhanced sediment deposition. The absence of barotropic trapping in their system is most likely due to a small U_r/U_t (~1/4).
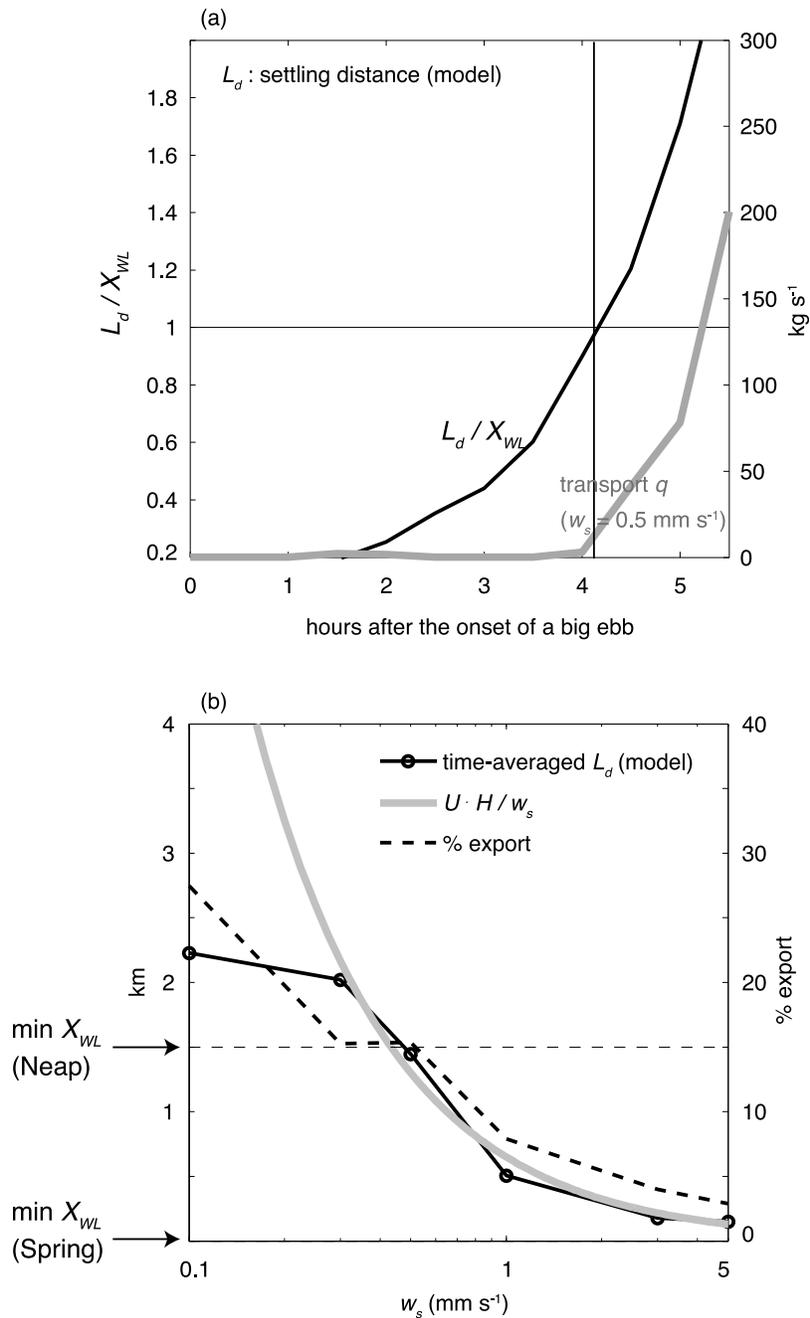
Figure 12. (a) Time series of the length scale ratio L_d/X_{WL} (black line, left y axis) and instantaneous transport q (gray line, right y axis) in the channel. The case with w_s of 0.5 mm s^{-1} is used as a representative example. Transport q is computed by equation (3). L_d is the settling distance (equation (4)), and X_{WL} is the cross-shore length of the intertidal zone (compare Figure 11). The vertical and horizontal lines indicate $L_d/X_{WL} = 1$, which coincides with the onset of sediment export. (b) Sensitivity of L_d averaged over a big ebb (black circle, left y axis) to settling velocity. An advective distance scaling of U_rH/w_s (gray line) is superposed. The river outlet velocity ($U_r = 1.2$ m s^{-1}) and depth ($H = 0.5$ m) are used in the scaling. The percentage of sediment export ($100 - \%$ trapping in Table 2) is also plotted as dashed line (right y axis). The minimum cross-shore length of the intertidal zone during spring and neap tides is 0 and 1.5 km, respectively.
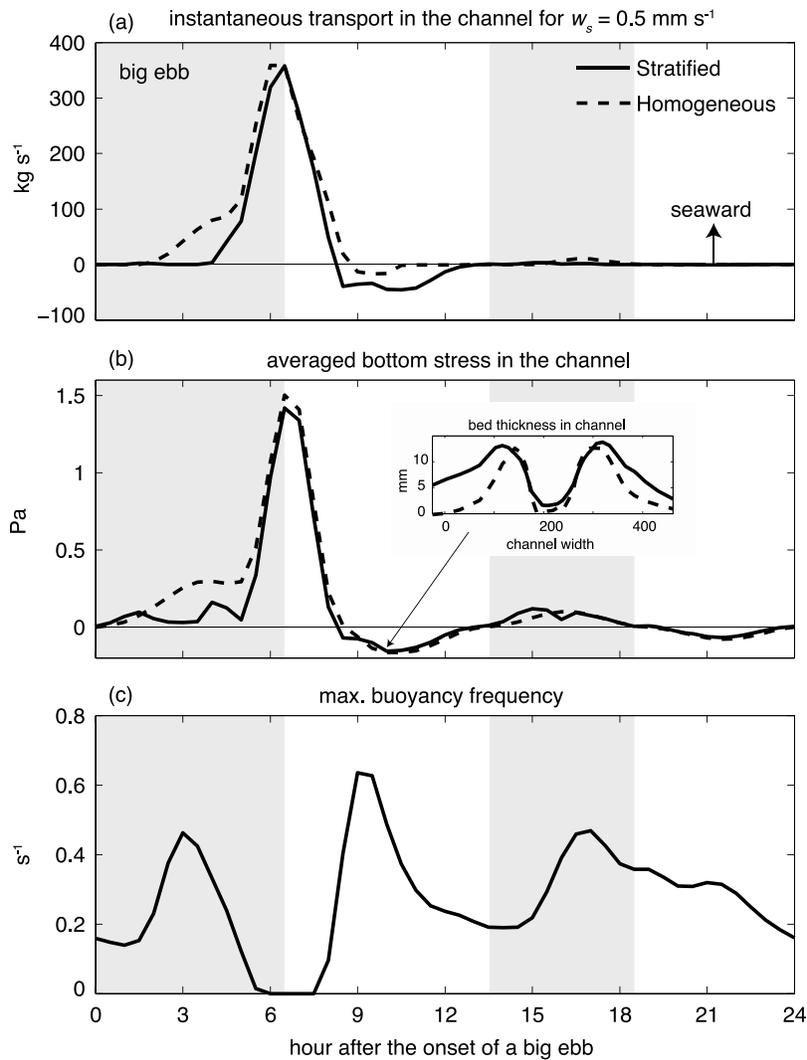
Figure 13. Time series of (a) transport, (b) averaged bottom stress, and (c) maximum buoyancy frequency in the channel for a typical mixed tide cycle during peak discharge, taken at the seaward edge of the intertidal zone. The case with w_s of 0.5 mm s^{-1} is taken as an example. The baseline (stratified) and homogeneous cases are donated by solid and dashed lines, respectively. Two gray shadings indicate big and small ebb. In Figure 13b, a snapshot of bed thickness in the channel is shown.

5.5. Sensitivities to Tidal Forcing and Channel Geometry

[36] Here we examine the sensitivity of our results to tidal range and tidal asymmetry. The sediment trapping and magnitude of transport rate are sensitive to changes in tidal range but relatively insensitive to varying tidal asymmetry (Table 2). Reducing tidal range (e.g., Neap tide case) leads to decreases in transport rate and export. For $w_s > 0.5$ mm s^{-1}, sediment input is completely trapped. This is because during neap tide condition the waterline does not retreat to the seaward boundary. Therefore, the minimum immersed cross-shore length of the intertidal zone, as indicated by a dashed horizontal line in Figure 12b, is still larger than the advective length for the sediment class of $w_s > 0.5$ mm s^{-1}, which then leads to 100% trapping. This sensitivity test indicates the importance of the minimum immersed cross-shore length of the intertidal zone for trapping.

[37] Surprisingly, applying flood- or ebb-dominated tidal forcing only leads to small changes in trapping. The ebb-dominated cases have slightly higher transport rates than the baseline and flood-dominated cases, but the differences are within 20%. Such results are explained by the observation that flood-ebb asymmetry primarily affects sediment fluxes on the flats and has negligible impacts on transport in the channel where the majority of the export takes place (compare Figure 8a). Applying pure semidiurnal tidal forcing (4 m M2 tides, not shown) leads to more export because of the higher barotropic tidal energy than the mixed tide cases. However, the export mechanism and the upper flat deposition patterns of the M2 tide case are essentially the same as the baseline cases.

[38] Sediment trapping and seaward transport rate for fast settling sediment classes are sensitive to changing channel geometry, but those for slow settling classes are not. We modify the channel width and depth while maintaining the

channel bankfull during peak discharge (footnotes h and i in Table 2). During big ebbs when export occurs, bottom stress is mainly controlled by the water depth. Compared with the baseline case, the averaged bottom stress increases by a factor of 1.5 in the narrower and deeper channel but decreases by 50% in the wider and shallower channel. For the slow settling sediment classes ($w_s < 1$ mm s^{-1}), the changes in seaward transport rate are relatively small (within 25%). This is due to the fact that the channel is largely scoured. Thus, further changes in bottom stress associated with different geometries do not significantly impact the seaward transport. In contrast, for the fast settling class ($w_s \geq 1$ mm s^{-1}), the transport rate increases twofold for a narrower and deeper channel but decreases to half of the baseline value for a shallower and wider channel. For this range of settling velocity, the channel is not sediment depleted. Increases in bottom stress with a narrow and deep channel therefore lead to more sediment export.

5.6. Long-Term Sediment Balance of the Intertidal Zone

[39] An unresolved issue of the present work concerns the morphological stability of the model results. Under a range of tidal forcings and channel geometries, we found that a majority of the total riverine sediment input remains in the intertidal zone (channel + flats) at the end of a characteristic discharge event. Using the total mass and the residual seaward transport rate after the event under spring tide conditions (i.e., maximum transport rate), we estimate that it would take at least 4–5 months for the finest sediment class to be completely flushed out of the system. The coarser classes would stay over a year. This means that the modeled intertidal zone is not under morphological equilibrium at a seasonal to annual time scale, based on fluvial inputs and tidal forcing conditions of the Skagit River. Also, the model-predicted accumulation of fine sediment is inconsistent with the sandy substrate observed from the repeated Skagit Bay nearshore mappings (Skagit Bay nearshore habitat mapping available from Skagit River System Cooperative at www. skagitcoop.org). The inconsistency presumably represents the time integration of a wide variety of forcing conditions and bathymetry differences between the idealized model and Skagit intertidal region. For example, the present model does not account for wind-wave forcing, which could keep sediment on the shallow flats in suspension during inundations and thereby enhance sediment export. The multiple channel network, which is observed on the Skagit Bay (compare Figure 1) but not modeled here, may provide more conduits for cross-shore sediment transport. However, evaluating an exhaustive list of factors contributing to the long-term stability of the intertidal zone is beyond the scope of present study. Future studies of this type should address the influence of wind waves on sediment transport on the intertidal zone in combination with the other forcing variables.

6. Summary

[40] We have investigated how different size classes of river-derived sediment are transported, exported and trapped on an idealized intertidal zone with a shallow tidal river channel. The model setup is motivated by the configuration of the intertidal region of the Skagit River mouth. This modeled system differs from most of the documented tidal flats in that river supplies not only influence stratification but also contributes a significant cross-shore transport. The tidal movement of the waterline separates the flow in this system into two regimes. Landward of the waterline, the channel flow is a seaward extension of the river, with velocities close to 1 m s^{-1} and high seaward-directed bottom stresses. Seaward of the waterline, the flow is governed by tides, with a maximum tidal velocity U_t of 0.4 m s^{-1}. As a result, the bottom stress is strongly ebb-dominated in the channel as the tidal flats drain during ebbs, and a strong barotropic convergence at the waterline is an important mechanism for sediment trapping.

[41] Sediment deposition patterns and mass budget are sensitive to settling velocity. The lateral (along-shore) sediment spreading is driven by a convergence between river and flooding tides and scales with an advective distance (settling time, H/w_s, multiplied by the lateral velocity). Therefore, fine sediment tends to deposit on the flats, whereas coarse sediment is confined to the channel. Residual sediment transport is landward on the flats, because of the settling lag effect. In the channel, the residual transport is seaward and is an order of magnitude larger than that on the flats, because of the influence of strong river flow. Sediment export to the offshore basin therefore mainly occurs in the channel during big ebbs and is controlled by a length scale ratio L_d/X_{WL}, where $L_d = U_r H/w_s$ is the distance over which sediment settles, and X_{WL} is the cross-shore length of the immersed portion of the intertidal zone. Sediment trapping then requires $L_d/X_{WL} < 1$. This means that complete trapping occurs when the advective distance of a sediment size class is less than the minimum cross-shore length of the intertidal zone. This underlines the importance of tidal range on sediment trapping, as tidal range controls X_{WL}. The trapping process is largely barotropic because it results from flow deceleration as sediment transits from fluvial to tidal regime. However, the presence of stratification contributes to additional trapping by reducing bottom stress.

[42] Under a range of tidal forcings and channel geometries, we found that a majority of the total riverine sediment input remains on the intertidal zone at the end of a characteristic discharge event. The excessive amount of trapped sediment and long-residence time hint that additional export mechanisms other than those by tides and river are required to maintain the morphological stability of the system.

References

Chen, S. N., and L. P. Sanford (2008), Lateral circulation driven by boundary mixing and the associated transport of sediments in idealized partially mixed estuaries, *Cont. Shelf Res.*, 29, 101–118, doi:10.1016/j.csr. 2008.01.1001.

Christie, M. C., K. R. Dyer, and P. Turner (1999), Sediment flux and bed level measurements from a macro tidal mudflat, *Estuarine Coastal Shelf Sci.*, 49, 667–688, doi:10.1006/ecss.1999.0525.

de Swart, H. E., and J. T. F. Zimmerman (2009), Morphodynamics of tidal intel systems, *Annu. Rev. Fluid Mech.*, *41*, 203–229, doi:10.1146/annurev.fluid.010908.165159.

Dyer, K. R., M. C. Christie, N. Feates, M. J. Fennessy, M. Pejrup, and W. van der Lee (2000), An investigation into processes influencing the morphodynamics of an intertidal mudflat, the Dollard Estuary, the Netherlands: I. Hydrodynamics and suspended sediment, *Estuarine Coastal Shelf Sci.*, *50*, 607–625, doi:10.1006/ecss.1999.0596.

Friedrichs, C. T., and D. G. Aubrey (1988), Non-linear tidal distortion in shallow well-mixed estuaries: A synthesis, *Estuarine Coastal Shelf Sci.*, *27*, 521–545, doi:10.1016/0272-7714(88)90082-0.

Friedrichs, C. T., and D. G. Aubrey (1996), Uniform bottom shear stress and equilibrium hypsometry of intertidal flats, in *Mixing in Estuaries and Coastal Seas, Coastal Estuarine Stud.*, vol. 50, edited by C. Pattiaratchi, pp. 405–429, AGU, Washington, D. C.

Geyer, W. R. (1993), The Importance of suppression of turbulence by stratification on the estuarine turbidity maximum, *Estuaries*, *16*, 113–125, doi:10.2307/1352769.

Geyer, W. R., P. S. Hill, and G. C. Kineke (2004), The transport, transformation and dispersal of sediment by buoyant coastal flows, *Cont. Shelf Res.*, *24*, 927–949, doi:10.1016/j.csr.2004.02.006.

Haidvogel, D. B., H. G. Arango, K. Hedstrom, A. Beckmann, and P. Malanotte-Rizzoli (2000), Model evaluation experiments in the North Atlantic basin: Simulations in nonlinear terrain-following coordinates, *Dyn. Atmos. Oceans*, *32*, 239–281, doi:10.1016/S0377-0265(00)00049-X.

Hoitink, A. J. F., P. Hoekstra, and D. S. van Maren (2003), Flow asymmetry associated with astronomical tides: Implications for the residual transport of sediment, *J. Geophys. Res.*, *108*(C10), 3315, doi:10.1029/2002JC001539.

Jones, W. P., and B. E. Launder (1972), The prediction of laminarization with a two-equation model of turbulence, *Int. J. Heat Mass Transfer*, *15*, 301–314, doi:10.1016/0017-9310(72)90076-2.

Kantha, L. H., and C. A. Clayson (1994), An improved mixed layer model for geophysical applications, *J. Geophys. Res.*, *99*, 25,235–25,266, doi:10.1029/94JC02257.

Kirby, R. (2000), Practical implications of tidal flat shape, *Cont. Shelf Res.*, *20*, 1061–1077, doi:10.1016/S0278-4343(00)00012-1.

Le Hir, P., W. Roberts, O. Cazaillet, M. C. Christie, P. Bassoulet, and C. Bacher (2000), Characterization of intertidal flat hydrodynamics, *Cont. Shelf Res.*, *20*, 1433–1459, doi:10.1016/S0278-4343(00)00031-5.

Postma, H. (1961), Transport and accumulation of suspended matter in the Dutch Wadden Sea, *Neth. J. Sea Res.*, *1*, 148–180, doi:10.1016/0077-7579(61)90004-7.

Pritchard, D., and A. J. Hogg (2003), Cross-shore sediment transport and the equilibrium morphology of mudflats under tidal currents, *J. Geophys. Res.*, *108*(C10), 3313, doi:10.1029/2002JC001570.

Ralston, D. K., and M. T. Stacey (2005), Longitudinal dispersion and lateral circulation in the intertidal zone, *J. Geophys. Res.*, *110*, C07015, doi:10.1029/2005JC002888.

Ralston, D. K., and M. T. Stacey (2007), Tidal and meteorological forcing of sediment transport in tributary mudflat channels, *Cont. Shelf Res.*, *27*, 1510–1527, doi:10.1016/j.csr.2007.01.010.

Roberts, W., P. Le Hir, and R. J. S. Whitehouse (2000), Investigation using simple mathematical models of the effect of tidal currents and waves on the profile shape of intertidal mudflats, *Cont. Shelf Res.*, *20*, 1079–1097, doi:10.1016/S0278-4343(00)00013-3.

Schuttelaars, H. M., and H. E. de Swart (1996), An idealized long-term morphodynamic model of a tidal embayment, *Eur. J. Mech. B Fluids*, *15*, 55–80.

Simpson, J. H., J. Brown, J. Matthews, and G. Allen (1990), Tidal straining, density currents, and stirring in control of estuarine stratification, *Estuaries*, *13*, 125–132, doi:10.2307/1351581.

Talke, S. A., and M. T. Stacey (2008), Suspended sediment fluxes at an intertidal flat: The shifting influence of wave, wind, tidal and freshwater forcing, *Cont. Shelf Res.*, *28*, 710–725, doi:10.1016/j.csr.2007.12.003.

van Straaten, J. M. J. U., and P. H. Keunen (1958), Tidal action as a cause of clay accumulation, *J. Sediment. Petrol.*, *28*, 406–413.

Warner, J. C., C. R. Sherwood, R. P. Signell, C. K. Harris, and H. G. Arango (2008), Development of a three-dimensional, regional, coupled wave, current, and sediment-transport model, *Comput. Geosci.*, *34*, 1284–1306, doi:10.1016/j.cageo.2008.02.012.

Yang, Z., and T. Khangaonkar (2009), Modeling tidal circulation and stratification in Skagit River estuary using an unstructured grid ocean model, *Ocean Modell.*, *28*, 34–49, doi:10.1016/j.ocemod.2008.07.004.

Yang, S., C. T. Friedrichs, Z. Shi, P. Ding, J. Zhu, and Q. Zhao (2003), Morphological response of tidal marshes, flats and channels of the outer Yangtze River mouth to a major storm, *Estuaries*, *26*, 1416–1425, doi:10.1007/BF02803650.

S.-N. Chen, W. R. Geyer, and D. K. Ralston, Applied Ocean Physics and Engineering, Woods Hole Oceanographic Institution, MS 10, Woods Hole, MA 02543, USA. (schen@whoi.edu)

C. R. Sherwood, U.S. Geological Survey, 384 Woods Hole Rd., Woods Hole, MA 02543, USA.